

Structural and Electrical Properties of Sprayed In₂S₃ Films on ITO/Glass Substrate

J. Koaib

Université de Gabès, Faculté des Sciences

N. Bouguila

Université de Gabès, Faculté des Sciences

M. Kraini (✉ mabrouk.karini@gmail.com)

Université de Gabès, Faculté des Sciences <https://orcid.org/0000-0002-2360-5606>

I. Halidou

Université Abdou Moumouni

K. Khirouni

Université de Gabès, Faculté des Sciences

C. Vázquez-Vázquez

Universidade de Santiago de Compostela

M. A. López-Quintela

Universidade de Santiago de Compostela

S. Alaya

Université de Gabès, Faculté des Sciences

Research Article

Keywords: In₂S₃ thin film, ITO substrate, Spray pyrolysis, Structural properties, Electrical properties

Posted Date: May 7th, 2021

DOI: <https://doi.org/10.21203/rs.3.rs-481705/v1>

License:  This work is licensed under a Creative Commons Attribution 4.0 International License.

[Read Full License](#)

Structural and electrical properties of sprayed In₂S₃ films on ITO/glass substrate

J. Koaib¹, N. Bouguila¹, M. Kraini^{1,*}, I. Halidou², K. Khirouni¹, C. Vázquez-Vázquez³, M.A. López-Quintela³, S. Alaya¹

¹Laboratoire de Physique des Matériaux et des Nanomatériaux appliqué à l'environnement, Université de Gabès, Faculté des Sciences, Cité Erriadh, Zrig, 6072 Gabès, Tunisia.

²Département de Physique, Faculté des Sciences et Techniques, Université Abdou Moumouni, BP 10662, Niamey Niger

³Laboratory of Magnetism and Nanotechnology (NANOMAG), Department of Physical Chemistry, Faculty of Chemistry, Universidade de Santiago de Compostela, 15782 Santiago de Compostela, Spain).

*Corresponding author: Mabrouk Kraini (M. Kraini)
E-mail: mabrouk.kraini@gmail.com

Abstract

In₂S₃ thin films were grown on indium tin oxide (ITO) glass substrate by chemical spray pyrolysis technique at 360°C. The structural analysis of the deposited films shows a combination of tetragonal and cubic structures. The average crystallite size is about 25 nm. The electrical properties of In₂S₃ thin films have been investigated in a wide frequency (40Hz-100MHz) and temperature (400 K-660 K) ranges.

We find that the electrical conductance of the In₂S₃ thin films is frequency and temperature dependent. The dc conductance shows a semi-conductor behavior for In₂S₃ films over the explored range of temperature and it follows the Arrhenius law with different activation energies. The variation of ac conductance and the frequency exponent 's' are explained by the correlated barrier hopping (CBH) model. The Nyquist plots of impedance exhibit semicircle arcs and an electrical equivalent circuit has been suggested to interpret the impedance results.

Keywords: In₂S₃ thin film; ITO substrate; Spray pyrolysis; Structural properties; Electrical properties

Introduction

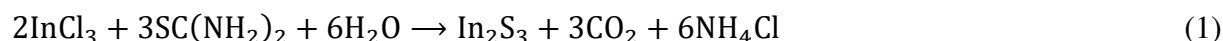
III-VI semiconductor thin films are attracting attention because of their interesting properties. In particular, indium sulfide (In_2S_3) thin films have attracted more attention because of their wide band-gap ranging from 2 to 3.7 eV [1-2], photoconductive behavior and controllable electrical properties [3-5]. It has been proved that In_2S_3 can be used in diverse applications such as solar energy conversion [6], photo detector [7], photo electrochemical cells [8] and gas sensors [9]. In_2S_3 thin films can be fabricated using spray pyrolysis [1, 10], ultrasonic dispersion [11], chemical bath deposition [12], physical vapor deposition [13], etc. In general, the growth technique affects the physical properties of In_2S_3 thin films. Many studies investigated a link between structural and optical properties of In_2S_3 thin films and their growth conditions as well as the nature of used substrates [14-18]. But the films electrical conductivity is not well studied. Indeed, only a few reports have been carried out on impedance spectroscopy of these semiconductor thin films. For example, in our previous works we investigated the ac conductivity properties of annealed In_2S_3 film [19] as well as the electrical conductivity of nickel doped In_2S_3 thin films deposited on glass substrates by spray technique [1]. Seyam [20] and Timoumi et al. [21] reported the dependence of ac conductivity on frequency of thermally evaporated In_2S_3 thin films.

In fact, the charge transport is very important characteristic for any thin film device. As known, the materials characteristics are mostly supervised by the charge carriers or defects creating over the processing itself. Therefore, it is important to pinpoint the charge carrier transport mechanism in these materials. In this paper, we investigate the frequency and temperature dependence on ac-conductance in order to determine conduction mechanism in In_2S_3 thin films deposited on indium tin oxide (ITO) substrate by spray pyrolysis technique.

2. Experiment

The In_2S_3 films were grown on ITO coated glass substrates by the spray pyrolysis technique. The solution was prepared by dissolving indium chloride (InCl_3) and thiourea

SC(NH₂)₂ with a ratio of S:In = 2.5. The InCl₃ concentration is 10⁻² mol l⁻¹. The formation of In₂S₃ is given by the following equation:



The obtained solution was sprayed onto the preheated ITO substrates maintained at 360°C. The ITO coated glass substrates were prepared in our laboratory by using the same spray pyrolysis technique and were used to carry out the electrical characterizations because of the highly conductivity of ITO material. The solution and gas flow rates were kept constant at 4 ml/min and 6 l/min, respectively. The nozzle-to-substrate distance was approximately 30 cm. The crystalline structure of the films was analyzed by X-ray diffraction (XRD) using Cu- α radiation (1.54186 Å) of a Philips PW1710 x-ray diffractometer. For electrical measurements, we have realized two-plots of gold by vacuum evaporation technique. The first one was deposited on In₂S₃ film as the top contact and the second one was deposited on ITO substrate as the bottom contact. An Agilent 4294A impedance analyzer was used to collect impedance measurements over a wide frequency range (40Hz-100MHz). We used a parallel circuit mode to measure the conductance (*G*). The voltage amplitude of the alternating signal was fixed at 200mV to get a best ratio of signal/noise. The sample was put in liquid nitrogen cryostat to vary the temperature between 400 K and 660 K.

3. Results and discussion

3.1. Structural analysis

Fig. 1 shows the XRD pattern of In₂S₃ thin film deposited on ITO-coated glass at 360°C. The pattern confirms that the elaborated films are polycrystalline in nature with the presence of sharp and well defined peaks. The diffraction peaks at 2 θ values of 33.53°, 43.96°, 48.06° and 50.81°, are correlated with the reflection of (400), (511), (440) and (600) planes of cubic β -In₂S₃ (JCPDS data file No. 73-1366). Whereas peaks at the positions of 14.4°, 27.63°, 60.45° and 70.58° which are assigned to (109), (431) and (444) planes respectively,

correspond to tetragonal β -In₂S₃ (JCPDS data file No. 41-1445). The (400) peak is the most intense one in the XRD pattern, which indicates that the β -In₂S₃ thin film has a preferred (400) growth direction and grow up approximately perpendicular to the seeded substrates. There are two diffraction peaks related to ITO substrates which can be indexed to the (222) and (400) planes of In₂O₃ phase.

The crystallite size and strain for the In₂S₃ thin film can be determined by Williamson–Hall plot as displayed in Fig. 2.

Williamson and Hall analysis is mainly used to separate these size and strain by combining the following two equations [22]:

$$\beta_{hkl} = \beta_S + \beta_D \quad (2)$$

$$\beta_{hkl} = \left(\frac{k\lambda}{D \cos \theta} \right) + (4\varepsilon \tan \theta) \quad (3)$$

Rearranging the equation gives:

$$\beta_{hkl} \cos \theta = \left(\frac{k\lambda}{D} \right) + (4\varepsilon \sin \theta) \quad (4)$$

where D is the crystallite size (nm), k is the shape factor ($k = 0.9$), λ is the wave length of the X-rays ($\lambda = 1.5406$ nm for Cu Ka radiation), θ is Bragg diffraction angle and β_{hkl} is the broadening of the hkl diffraction peak measured at half of its maximum intensity (in radians).

A plot is drawn by taking $4 \sin \theta$ along X-axis and $\beta_{hkl} \cos \theta$ along Y-axis as shown in Fig. 2.

The strain and the crystallite size are, respectively, extracted from the slope and the intercept of the linear fit made to the plot. The obtained values of the crystallite size and the strain are found to be 25 nm and 2.71×10^{-3} , respectively. It is noticed that the strain in the film is tensile ($\varepsilon > 0$) [23].

The value of dislocation density (δ) was obtained using the relation [24]:

$$\delta = \frac{1}{D^2} \quad (5)$$

The calculated value of dislocation density (δ) is 15.5×10^{10} lines.cm⁻².

3.2. DC conductance (G_{dc}) and activation energy

Fig. 3 shows the dc conductance plotted as a function of frequency for the In₂S₃ thin film deposited on ITO substrate. The conductance increases with temperature. Such result reflects a semiconductor behavior along the entire explored temperature range [25]. In fact, as the temperature is enhanced more charge carriers surmount the activation energy barrier and participate in the electrical conductivity [26].

The experimental data of electrical conductance are well adjusted by Arrhenius relation as described by the following equation [27]:

$$G_{dc} = G_0 \exp\left(\frac{-E_a}{K_B T}\right) \quad (6)$$

where G_0 is a pre-exponential factor, E_a is the activation energy of dc-conductivity, k_B is the Boltzmann constant and T is the absolute temperature.

The thermal evolution of Log (G_{dc}) versus $1000/T$ is illustrated in Fig. 4. Three regions are shown and separated by two discontinuities in the temperature range 480 and 540 K. The deduced activation energy values in region I, II and III are equal to 0.711 eV, 1.42 eV and 0.981 eV, respectively. The variation in the activation energies values can be due to change in the type of conduction or to the change in the charge carrier type (electron or hole) [28].

3. 3. AC conductance (G_{ac})

Fig. 5 shows the frequency (ω) dependence of the ac-conductance at different temperatures. It is noticeable that ac conductance spectra can be divided into three parts. The first is at low frequency, in such region, the conductance varies slightly with frequency and increases with temperature. However, at intermediate frequencies, the conductance increases linearly with frequency. This rise of conductance is attributed to hopping mechanism that occurs by the influence of an applied electrical field. In this region, the conductance increases proportionally to ω^s with increasing frequency. The third region is at higher frequencies where the conductance decreases with increasing frequency. So, for this sample, metallic behavior dominates for temperatures $> 610K$. This might be due to the enhancement of resistive character as a result of the polaron scattering and the larger amplitude of vibration at high temperature [29].

In addition, we noted that at any one of these selected frequency, G_{ac} increases with the increases in temperature, which emphasizes the semiconductor behavior of this sample [30]. In fact, this rise of ac conductance is attributed to the increasing in the numbers of charge carriers and mobility [31].

In the other hand, the experimental data of ac-conductance are well described by the equation:

$$G_{ac}T = B \exp\left(\frac{-E_a}{K_B T}\right) \quad (7)$$

E_a is the activation energy of conduction mechanism and B is a temperature-dependent constant.

The variation of $\text{Log } G_{ac}T$ versus $1000/T$ can be splitted into two regions; the first region which is relatively to the temperatures below a certain temperature symbolizing by T_d and the second region which is relatively to the temperature above T_d as depicted in Fig. 6.

In the region 1, the ac-conductivity increases with rising frequency and temperature. Such behavior may be related to the ac-hopping conduction of the localized carriers [32]. While in region 2, the conductance is independent of frequency. The obtained activation energy (E_a) values are reported in the Table 1. As noted, the activation energy involved in ac conductivity is lower than the activation energy attributed to the dc-conductance (region II of Fig. 4). Knowing that for dc-conductivity, the charge carriers look for the easiest path between ions but in sometimes, the paths which are chosen, comprises a large distance between ions in the hopping mechanism. Other hopping sites are ready in ac-conductance; hence the activation energy deduced from ac-conductance is lower than the one of dc-conductance.

In addition, we notice that the activation energy (E_a) decreases with increasing frequency, such behavior is due to the increment of the applied field frequency which improved charge carriers to jump between localized states [33].

To identify the conduction mechanism of our sample, various theoretical models proposed by Elliot et al [34] are used to link the conduction mechanism of ac-conductivity with the temperature behavior of s exponent. The values of the s exponent were deduced from the slopes of straight lines in Fig. 5. The evolution of frequency exponent 's' with temperature is depicted in Fig. 7. It is evident that the values of s decrease with increasing temperature in three regions which is in good agreement with the predicted values of the correlated barrier-hopping (CBH) model which explains the hopping of charge carriers between sites separating by the potential barrier [35].

According to this model of conduction (CBH)[36], we have used the following equation proposed by Mott and Davis to calculate the maximum barrier height (W_M):

$$s = 1 - (6 k_B T / W_m) \quad 8)$$

The potential barrier W_M was calculated from the linear fit of the curve (1-s) as a function of temperature which is illustrated in Fig. 8.

The obtained values of W_M in the three regions I, II and III are $W_{m1}(I) = 0.093$ eV, $W_{m2}(II) = 0.601$ eV and $W_{m3}(III) = 0.141$ eV, respectively.

3. 4. Impedance measurement

Fig. 9 represents the variation of the real part of impedance Z' with frequency for the In_2S_3 thin film deposited on ITO substrate. One can see that Z' has large values at low frequencies and temperatures, and then Z' decreases with increasing the temperature and frequency indicating an improvement in ac conductance. However, at high frequencies, it merges for all temperatures which confirm the presence of space charge polarization in our material.

The temperature dependence of real part of impedance can be explicated by deducing the average normalized change (ANC) which is considered to be the intrinsic response of the sample. The ANC is calculated from the quantity $(\Delta Z' / \Delta f) / Z_0$, where $\Delta Z'$ is the difference between the Z' value (Z'_{low}) at low frequency (f_{low}) and its value Z'_{high} at high frequency (f_{high}), i.e. $\Delta Z' = Z'_{\text{low}} - Z'_{\text{high}}$ [37], $\Delta f = f_{\text{low}} - f_{\text{high}}$ and Z_0 is the value of Z' at frequency equal to zero. The last quantity is determined from the extrapolation of the plateau to low frequency. The ANC variation with the temperature is represented in Fig. 10. The ANC is temperature independent in the low temperatures region then it shows a decreasing trend with increasing temperature. This behavior proves the presence of different conduction process in low and high temperature regions, and also suggests that the density of trapped charges decreases with increasing temperature [38].

The slope of the ANC derivative at any temperature provides us information about the number of released trapped charges, which is dependent upon the density of trapped charges

state. Fig. 11 shows the $\frac{d(ANC)}{dT}$ as a function of temperature. A change in the slope of the derivative of ANC at around 600 K was noted, indicating that the available density of trapped charge states disappeared around 600 K, which is in a good agreement with the conductance analysis reported by [39].

Fig. 12 represents the variation of the imaginary part of impedance Z'' with frequency at different temperatures. As noted in this figure, the evolution of Z'' is dominated by a single peak which shifts to higher frequencies with the increase of temperature, confirming the existence of a relaxation phenomenon in the system. Furthermore, a considerable broadening of the peaks with increase in temperature affirms the existence of a temperature dependent electrical relaxation phenomenon. Further, the height of the detected peaks decreases when the temperature increases. Such behavior suggests that the charge carriers existed in this material, are thermally activated.

Further, the impedance data of Z'' was used to evaluate the relaxation time (τ) of the electrical phenomena in the material. The τ values are determined from the peak position of Z'' versus frequency plot using the relation $2\pi f_r \tau = 1$, where f_r is the relaxation frequency. Fig. 13 illustrates the plot of $\ln(\tau)$ against $1000/T$ using Arrhenius model. This plot reveals two change of slope at 480 K and 540 K. The calculated activation energies from the linear fit of the data points are found to be 0.71, 1.19 and 2.156 eV in the regions (I), (II) and (III), respectively. It was detectable that the values of activation energies deduced from relaxation time in the regions (I) and (II) are near to the values estimated from conductance spectrum, which indicates that transport property is owing to hopping mechanism [40]. Besides, the activation energy of the relaxation process (region III) is higher than that of the conduction mechanism, suggesting that the relaxation process does not govern the conduction mechanism [41]. Indeed, the all types of carriers contributed to the conduction at low temperatures, cannot contribute to the relaxation process [42].

The Cole-Cole plots at different temperatures of the In₂S₃ thin film deposited on ITO substrate are exhibited in Fig. 14. These plots show semi-circle arcs below the real axis suggesting a non-Debye type relaxation phenomenon of charge carriers [43]. The shape of the semi-circle patterns is independent of the temperature. Moreover, the maximum of the semi-circles displaces to higher frequencies and their diameters decrease with rise in temperature, which proves that electrical conduction process is thermally activated, and relaxation times distribution.

To associate the electrical properties with the microstructure of the sample, the experimental data are fitted using Zview software [44]. The best fit is reached when using an equivalent circuit composed by a parallel combination of grain resistance (R_g) and constant phase element impedance of grain (CPE_g) associated in series with a parallel combination grain boundaries resistance (R_{gb}) and constant phase element impedance of grain boundaries (CPE_{gb}) as shown in Fig. 15.

The CPE impedance is expressed as:

$$Z_{CPE} = 1/Q (j\omega)^\alpha \quad (9)$$

where Q is the capacitance value of the CPE impedance and α ($0 < \alpha < 1$) represents the deviation from Debye's model.

The fitting results are listed in Table 2. It is evident that as the temperature increases the grain resistance decreases until becoming negligible at 500 K. We note that the grain boundary resistance values are higher than that of grain resistance. Such result can be ascribed to the presence of dangling bonds on the grain boundaries, playing an important role in charge carrier traps and barrier layer width which declines when the temperature rises and also to the disorder of the atomic arrangement near the grain boundary area which improves significantly the electron scattering [45].

4. Conclusion

We have deposited In_2S_3 thin films on ITO substrate at 360°C by spray pyrolysis technique. The XRD patterns show that the In_2S_3 films are well crystallized in mixed phase of both cubic and tetragonal structure. The films crystallite size is estimated to 25 nm. The electrical characterization illustrates that the electrical conductivity enhances with increasing temperature, while this enhancement declines after 610 K where a metallic behavior appears. The ac-conductance spectrum follows Jonscher's power law. The temperature dependence of the exponent 's' proves that a correlated barrier hopping (CBH) is the most appropriate model to identify the electrical conduction mechanism of the film. The impedance analysis reveals the thermally activated dependence on temperature, which is in good coherence with the conductivity analysis. Nyquist plots confirm the presence of grains and grain boundaries that are modeled by an equivalent circuit.

Acknowledgments

This work was supported by Tunisian Ministry of Higher Education and Scientific Research, partly supported by the projects HP-NANOBIO Project PID2019-111163RB-I00, granted by Spanish Ministry of Science, Spain. The authors also thanks the use of RIAIDT-USC analytical facilities.

References

- [1] M. Kraini, N. Bouguila, N. Moutia, J. El Ghoul, K. Khirouni, and C. Vázquez-Vázquez, J. Mater. Sci: Mater Electron. 29 (2017) 1888–1906.
- [2] N. Bouguila, M. Kraini, A. Timoumi, I. Halidou, C. Vázquez-Vázquez, M.A. López Quintela, S. Alaya, J. Mater. Sci. 26 (2015) 7639–7648.
- [3] S.S. Wang, F.J. Shiou, C.C. Tsao, S.W. Huang, C.Y. Hsu, Mater. Sci. Semicond. Process. 16 (2013) 1879–1887.
- [4] G.R. Gopinath, R.W. Miles, K.T.R. Reddy, Energy Procedia. 34 (2013) 399–406.
- [5] T.T. John, S. Bini, Y. Kashiwaba, T. Abe, Y. Yasuhiro, C.S. Kartha, K.P. Vijayakumar, Semicond. Sci. Technol. 18 (2003) 491–500.
- [6] Y.J. Hsiao, Ch.H. Lu, L.W. Ji, T.H. Meen, Y.L. Chen, H.P. Chi, Nanoscale Res. Lett. 9 (2014) 32–38.
- [7] R.A. Ismail, N.F. Habubi, M.M. Abbod, Opt. Quantam. Electron. 48 (2016) 455–468.
- [8] R.S. Becker, T. Zheng, J. Elton, M. Saeki, Sol. Energy Mater. 13 (1986) 97–107.
- [9] R. Souissi, N. Bouguila, A. Labidi, Sensors and Actuators B 261 (2018) 522–530
- [10] M. Mathew, R. Jayakrishnan, P.M.R. Kumar, C. S. Kartha, K.P. Vijayakumar, T. Abe, Y. Kashiwaba, J. Appl. Phys. 100 (2006) 033504-1– 033504-8
- [11] Z. Li, X. Tao, Z. Wu, P. Zhang, Z. Zhang, Ultrason. Sonochem. 16 (2009) 221–224.
- [12] B. Asenjo, C. Sanz, C. Guillén, A.M. Chaparro, M.T. Gutiérrez, J. Herrero, Thin Solid Films. 515 (2007) 6041-6044.
- [13] N. Barreau, J.C. Berne`de, C. Deudon, L. Brohan, S. Marsillac, Thin Solid Films. 241(2002) 4-14.

- [14] N. Bouguila, M. Kraini, A. Timoumi, I. Halidou, C. Vázquez Vázquez, M.A. López-Quintela, S. Alaya, *J. Mater. Sci: Mater Electron* 26 (2015) 7639-7648.
- [15] D. Soro, B. Fofana, M. Sidibé, B. Aka, B. Mari, S. Touré, *Int. Res. J. Eng. and Tech (IRJET)*, 4 (2017) 686-691.
- [16] S. Belgacem, R. Bennaceur, *Revue. Phys. Appl* 25 (1990) 1245–58.
- [17] N. Kamoun, N. Jebbari, S. Belgacem, R. Bennaceur, *J. Appl. Phys.* 91 (2002) 1952-1958.
- [18] T. Sall, B. M. Soucase, M. Mollar, B. Hartitti, M. Fahoume, *J. Phys and Chem Solids* 76 (2015) 100–104.
- [19] N. Bouguila, I. Najeh, N. Ben Mansour, H. Bouzouita, S. Alaya, *J Mater Sci: Mater Electron.* 26 (2015) 6471-6477.
- [20] M.A.M. Seyam, A.E. Bekheet, A. Elfalaky, *Eur. Phys. J. Appl. Phys.* 16 (2001) 99-104.
- [21] A. Timoumi, *Int. J. Adv. Res. Electr. Electron. Instrum. Eng.* 2 (2013) 5207–5212.
- [22] A. Khorsand Zak, W.H.A. Majid, M.E. Abrishami and R. Yousefi, *Solid State Sci.* 13 (2011) 251–256.
- [23] J. Koab, N. Bouguila, M. Kraini, A. Mhamdi, I. Halidou, M. Ben Salem, H. Bouzouita, S. Alaya, *J Mater Sci: Mater Electron.* 27 (2016) 9216–9225.
- [24] A. Arfaoui, B. Ouni, S. Touihri, A. Mhamdi, A. Labidi, T. Manoubi, *Optical Materials.* 45 (2015) 109–120.
- [25] R. Lahouli, J. Massoudi, M. Smari, H. Rahmouni, K. Khirouni, E. Dhahri and L. Bessais, *RSC Adv.* 9 (2019) 19949–19964.
- [26] M. Caglar, S. Ilican, Y. Caglar, F. Yakuphanoglu, *Applied Surface Science*, 255 (2009) 4491–4496.
- [27] W. Wang, X.J. Wang, J. Zhu, X.Y. Mao, X.B. Chen, *Chin. Phys. Lett.* 26 (2009) 047701.
- [28] Y. Ben Taher, A. Oueslati, K. Khirouni, M. Gargouri, *J. Mater. Res. Bull.* 78 (2016) 148–157.

- [29] H. Rahmouni, M. Smari, C. Boutheina, E. Dhahri and K. Khirouni, Dalton Trans. 44(2015)10457–10466.
- [30] L. Essaleh, S. Amhil, S.M. Wasim, G. Marin, E. Choukri, L. Hajji, Physica E 99 (2018) 37–42.
- [31] J. Shanker, B. Vittal Prasad, M. Buchi Suresh, R. Vijaya Kumar, D. Suresh Babu, MRB 94 (2017) 385–398.
- [32] G. F. Pike, Phys. Rev. B. 6 (1972)1572–1580.
- [33] A. A. Ebnalwaled, International Journal of Basic & Applied Sciences IJBAS-IJENS 11(2011)194–207.
- [34] S. R. Elliot, J. Adv. Phys. 36 (1987)135–217.
- [35] A.R. Long, Adv. Phys. 31 (1982) 553–637.
- [36] R. Megha, S. Kotresh, Y. T. Ravikiran, C. H. V. V. Ramana, S. C. V. Kumari and S. Thomas, Compos. Interfaces. 24 (2016)55–68.
- [37] M. Nadeem, M.J. Akhtar, M.N. Haque, Solid State Commun. 145 (2008) 263–266.
- [38] M. Shah, M. Nadeem, M. Idrees, M. Atif, M.J. Akhtar, J. Magn. Magn. Mater. 332 (2013) 61–66.
- [39] I.S. Yahia, J. Acta Physica Polonica A. 125 (2014) 1167–1171.
- [40] T. Rhimi, M. Toumi, K. Khirouni, S. Guermazi, J. Alloys Compd. 714 (2017) 546–552.
- [41] V. Senthil, T. Badapanda, A. Chithambararaj, A. Chandra Bose, A.K. Mohapatra and S. Panigrahi, J.Polym. Res. 19 (2012) 9898–9906.
- [42] R. Mbarki, A.H. Hamzaoui, A. Minif, Eur. Phys. J. Appl. Phys. 69 (2015)10402–10408.
- [43] B. Deka, S. Ravi and D. Pamu, Ceram. Int. 43 (2017) 10468–10477.

[44] D. Johnson, *ZView: a software program for IES analysis. Version 2.8.* (Scriber Associates, Inc, Southern Pines, 2008).

[45] R. Jemaï, R. Lahouli, S. Hcini, H. Rahmouni, K. Khirouni, J. Alloys . *Compd.* 705 (2017) 340–348.

Tables and Figures

Table 1: Activation energy values of In_2S_3 film deposited on ITO substrate at different frequencies.

Table 2: Fitting parameters of the Nyquist diagram at different temperatures for In_2S_3 film deposited on ITO substrate.

Figure 1: XRD patterns of In_2S_3 film deposited on ITO substrate.

Figure 2: Williamson–Hall analysis of In_2S_3 films deposited on ITO substrate assuming UDM. Fit to the data, the strain is extracted from the slope and the crystallite size is extracted from the y-intercept of the fit.

Figure 3: Plot of DC conductance versus temperature for In_2S_3 thin film deposited on ITO substrate.

Figure 4: Variation of $\log(G_{dc})$ as a function of $(1000/T)$ for In_2S_3 film deposited on ITO substrate.

Figure 5: Frequency dependence of ac conductance for In_2S_3 film deposited on ITO substrate.

Figure 6: Temperature dependence of ac conductance at different frequency (1kHz, 20kHz et 100kHz) of the In_2S_3 film deposited on ITO substrate.

Figure 7: Variation of frequency exponent (s) with temperature of In_2S_3 film deposited on ITO substrate.

Figure 8: Variation of $(1-s)$ with temperature of In_2S_3 film deposited on ITO substrate.

Figure 9: Variation of the real part Z' of impedance as a function of frequency at different temperatures for In_2S_3 film deposited on ITO substrate.

Figure 10: Average normalized change ANC with temperature for In_2S_3 film deposited on ITO substrate.

Figure 11: Variation of $d(\text{ANC})/d(T)$ with temperature for In_2S_3 film deposited on ITO substrate.

Figure 12: Variation of the imaginary part Z'' of impedance as a function of frequency at different temperatures for In_2S_3 film deposited on ITO substrate.

Figure 13: Arrhenius plot of time relaxation.

Figure 14: Complex impedance spectrum ($-Z''$ vs. Z') of In_2S_3 film deposited on ITO substrate.

Figure 15: Results of fitting of the Nyquist diagram and equivalent circuit model for In_2S_3 film deposited on ITO substrate.

Figures

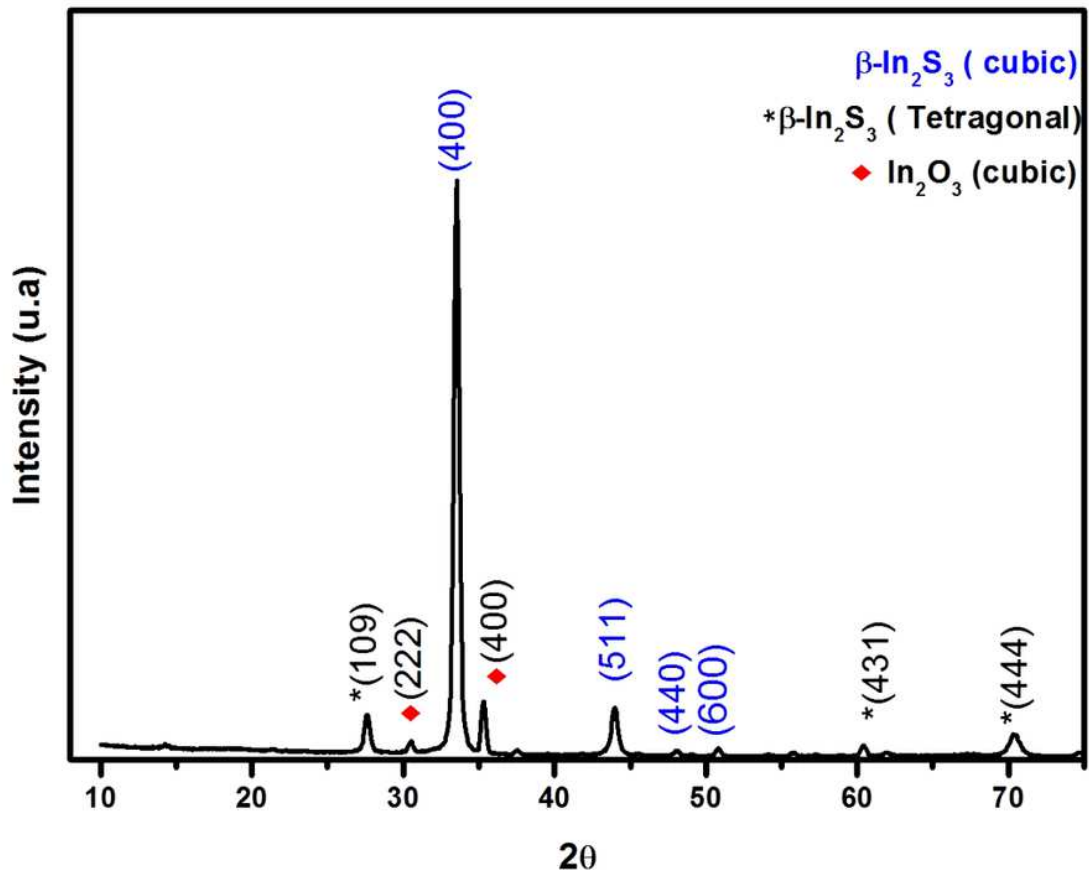


Figure 1

XRD patterns of In_2S_3 film deposited on ITO substrate.

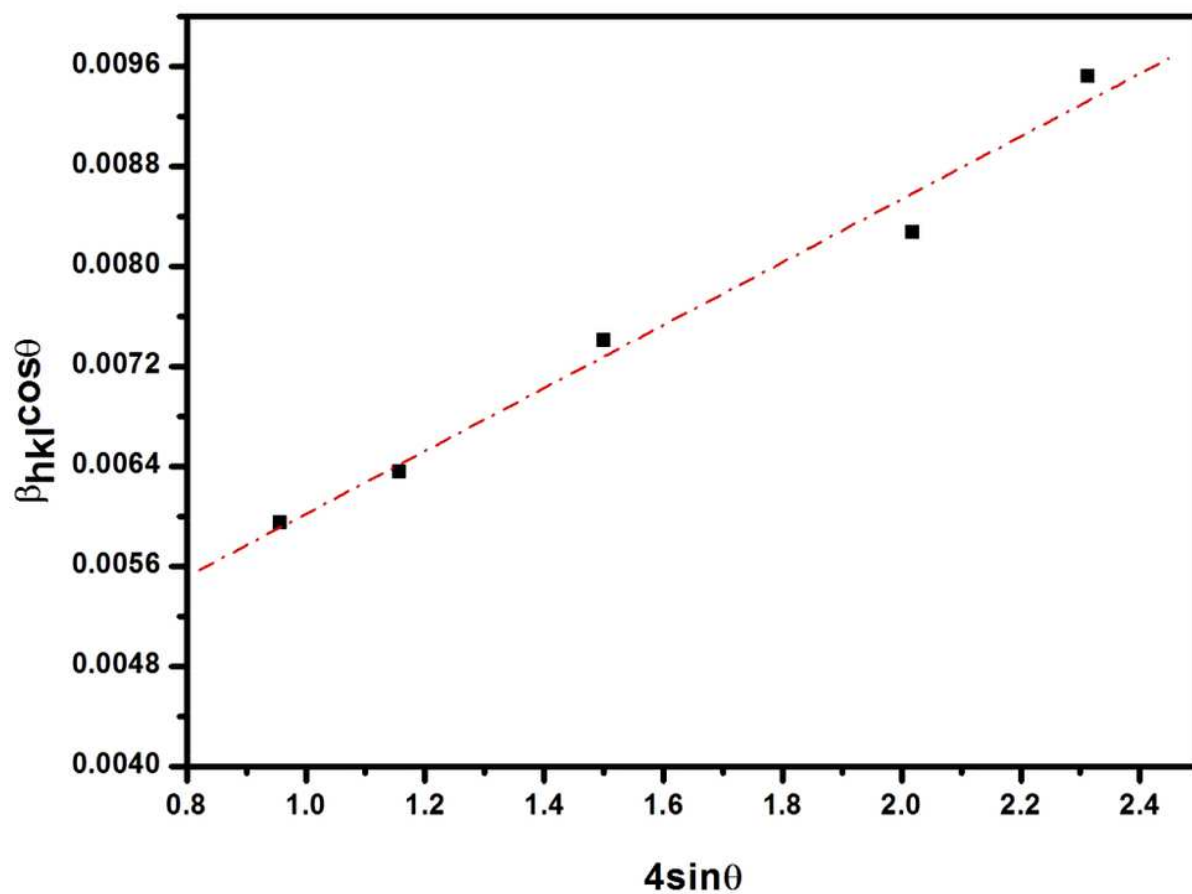


Figure 2

Williamson-Hall analysis of In_2S_3 films deposited on ITO substrate assuming UDM. Fit to the data, the strain is extracted from the slope and the crystallite size is extracted from the y-intercept of the fit.

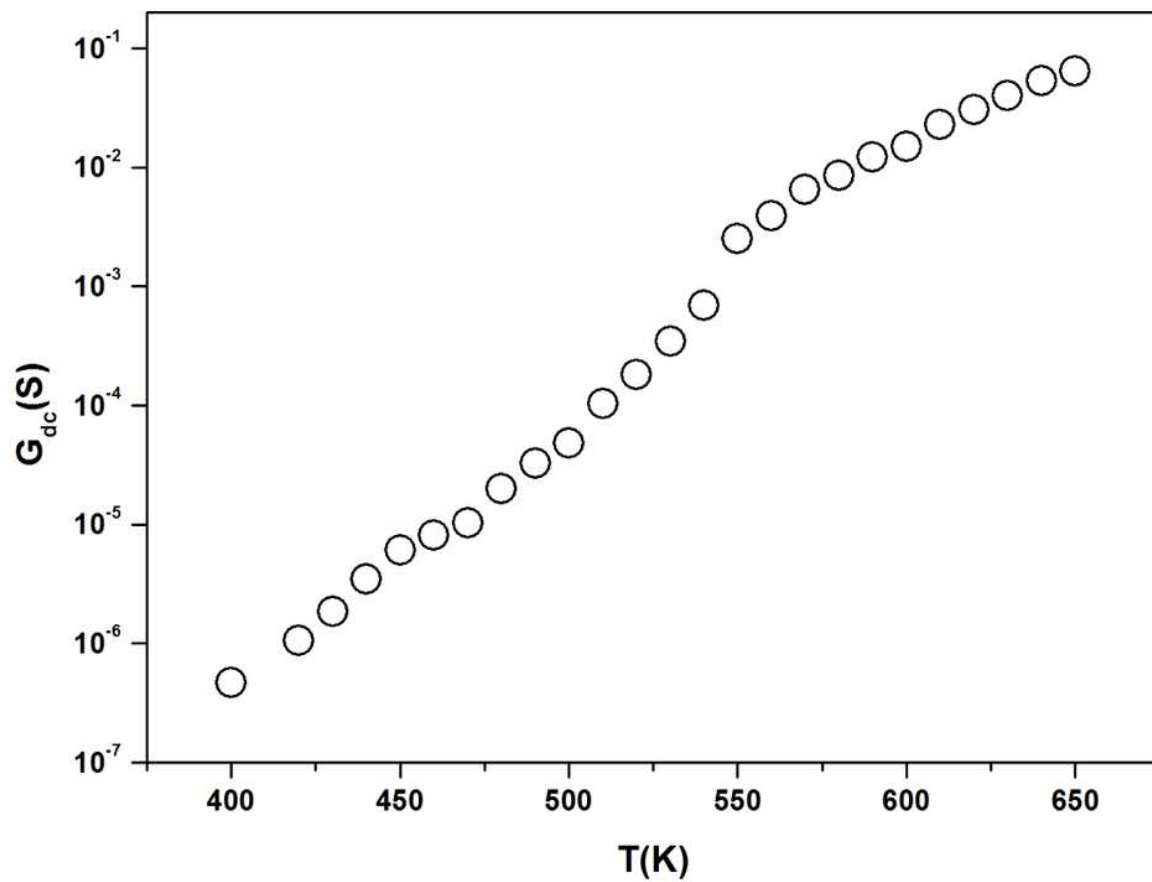


Figure 3

Plot of DC conductance versus temperature for In₂S₃ thin film deposited on ITO substrate.

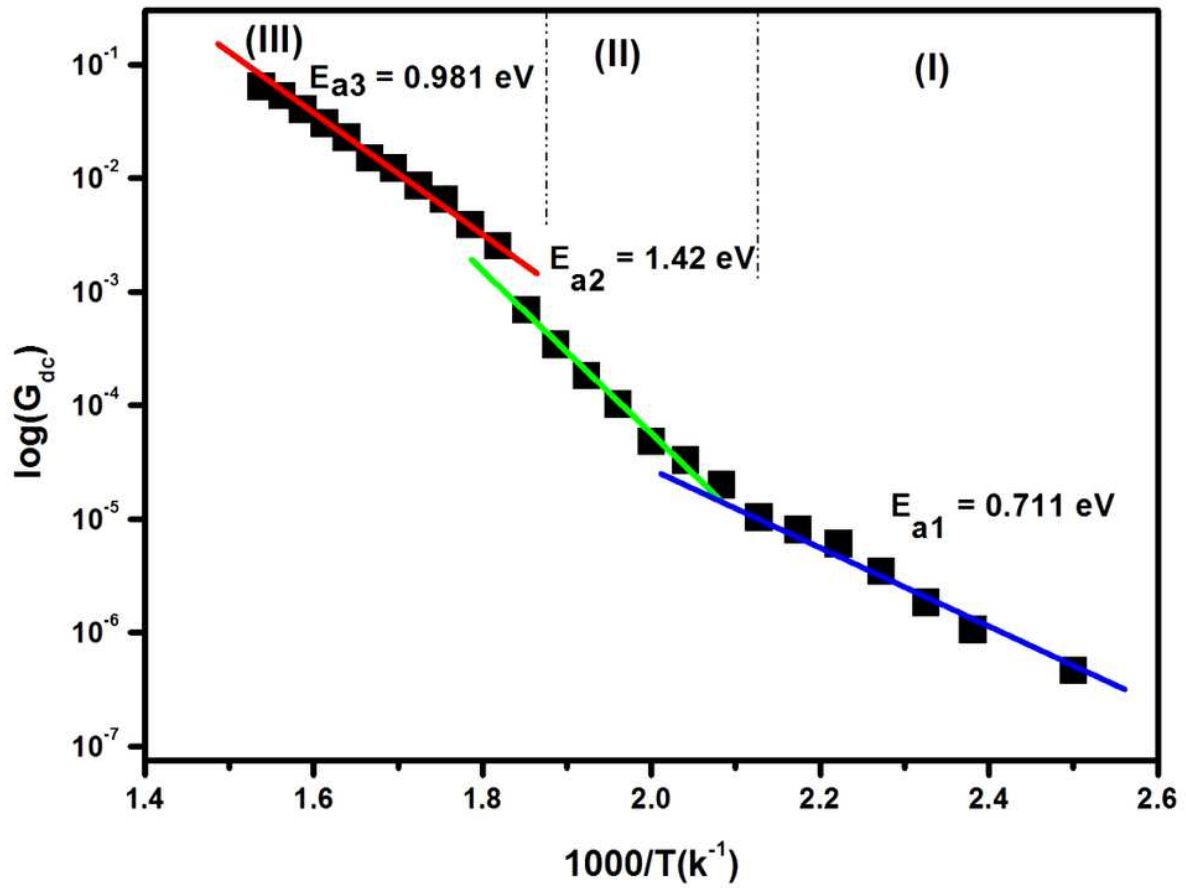


Figure 4

Variation of $\log(G_{dc})$ as a function of $(1000/T)$ for In_2S_3 film deposited on ITO substrate.

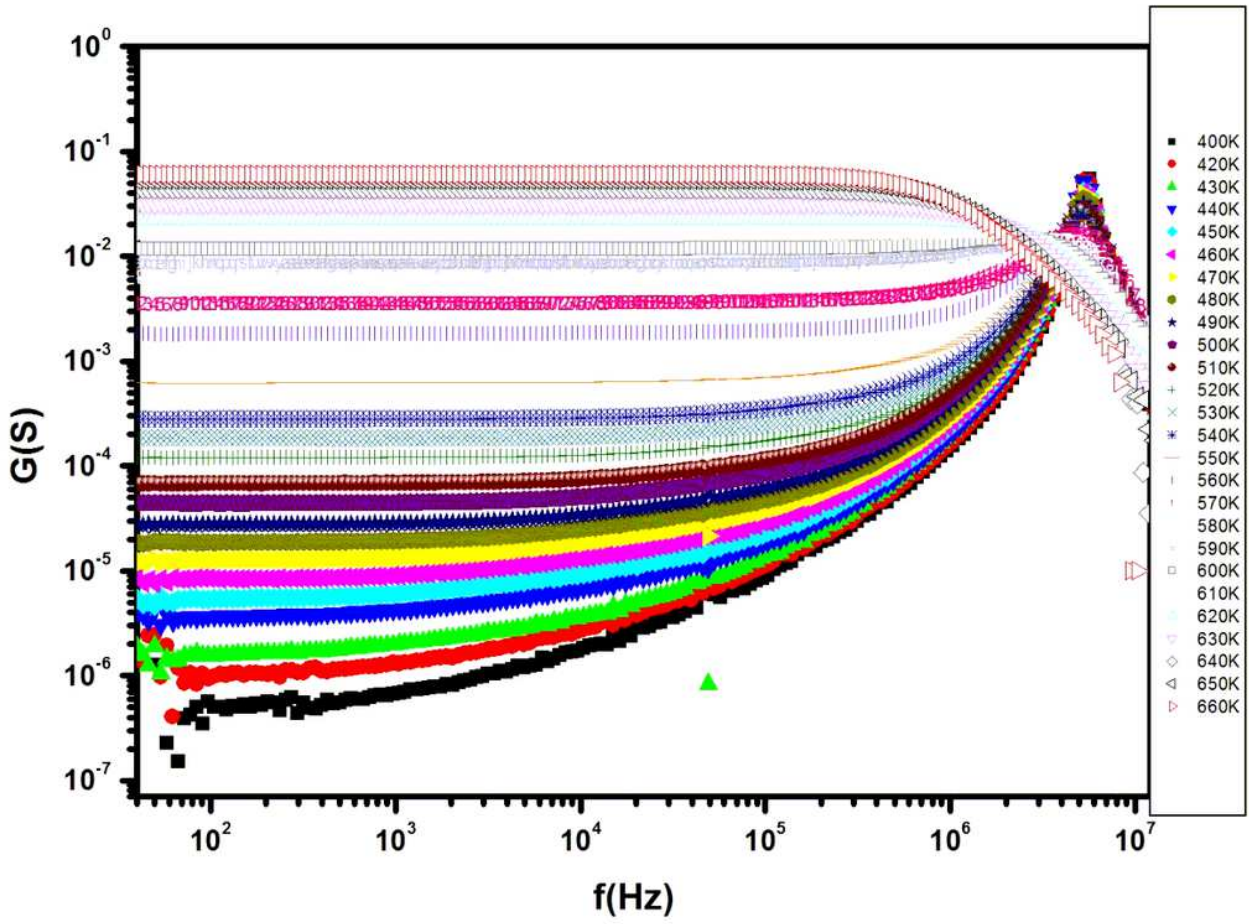


Figure 5

Frequency dependence of ac conductance for In₂S₃ film deposited on ITO substrate.

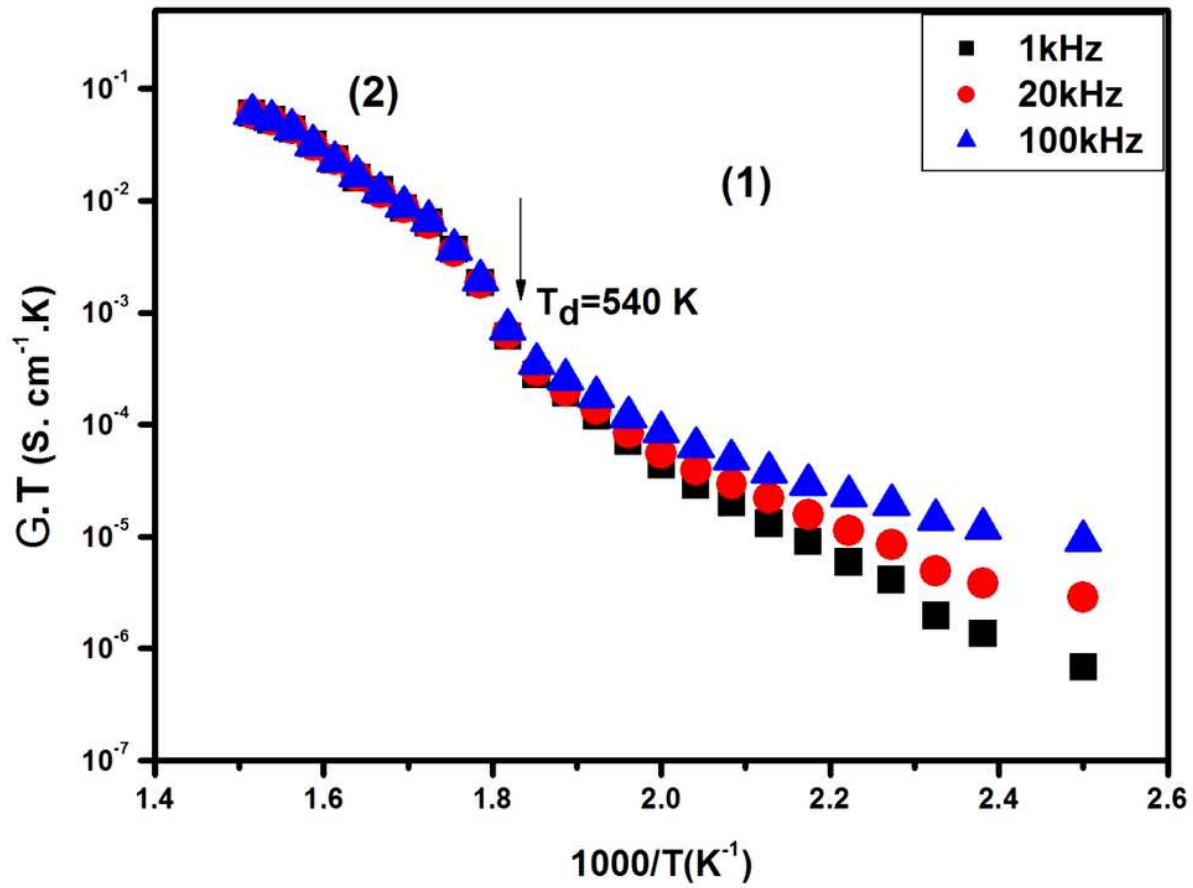


Figure 6

Temperature dependence of ac conductance at different frequency (1kHz, 20kHz et 100kHz) of the In_2S_3 film deposited on ITO substrate.

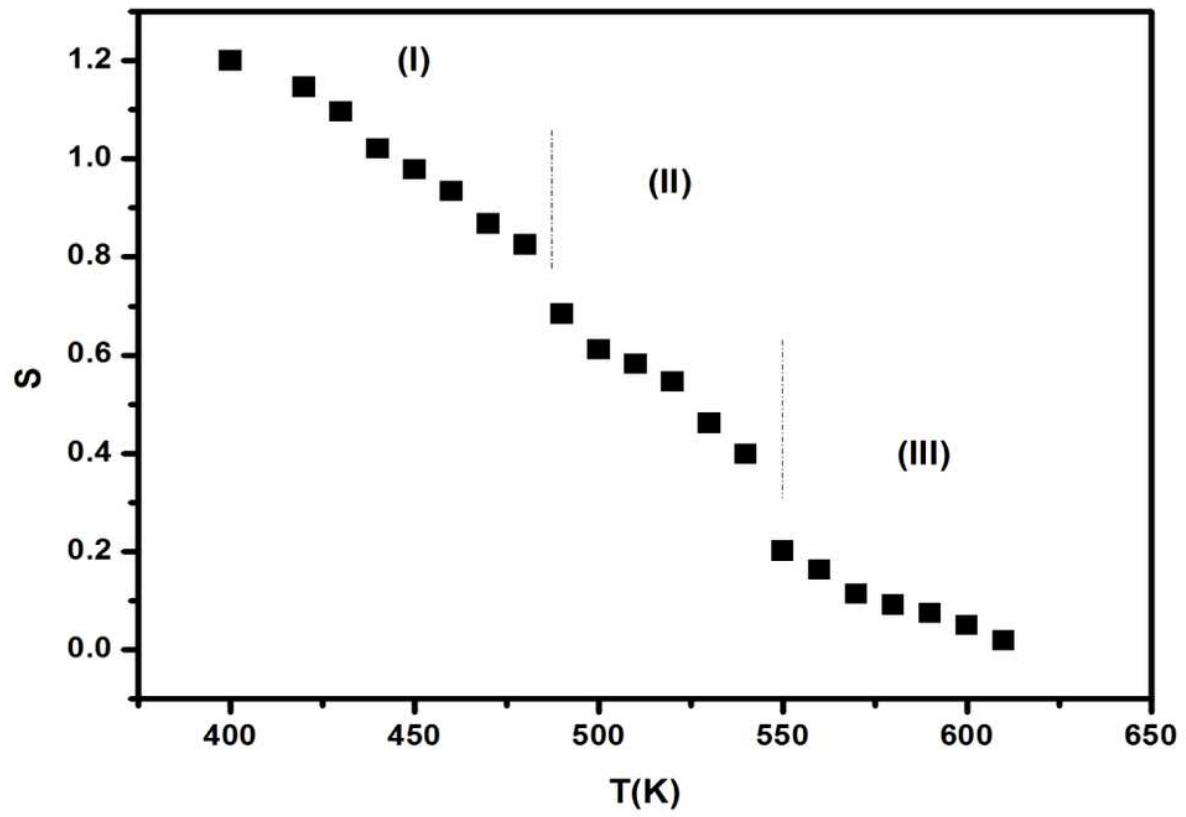


Figure 7

Variation of frequency exponent (s) with temperature of In₂S₃ film deposited on ITO substrate.

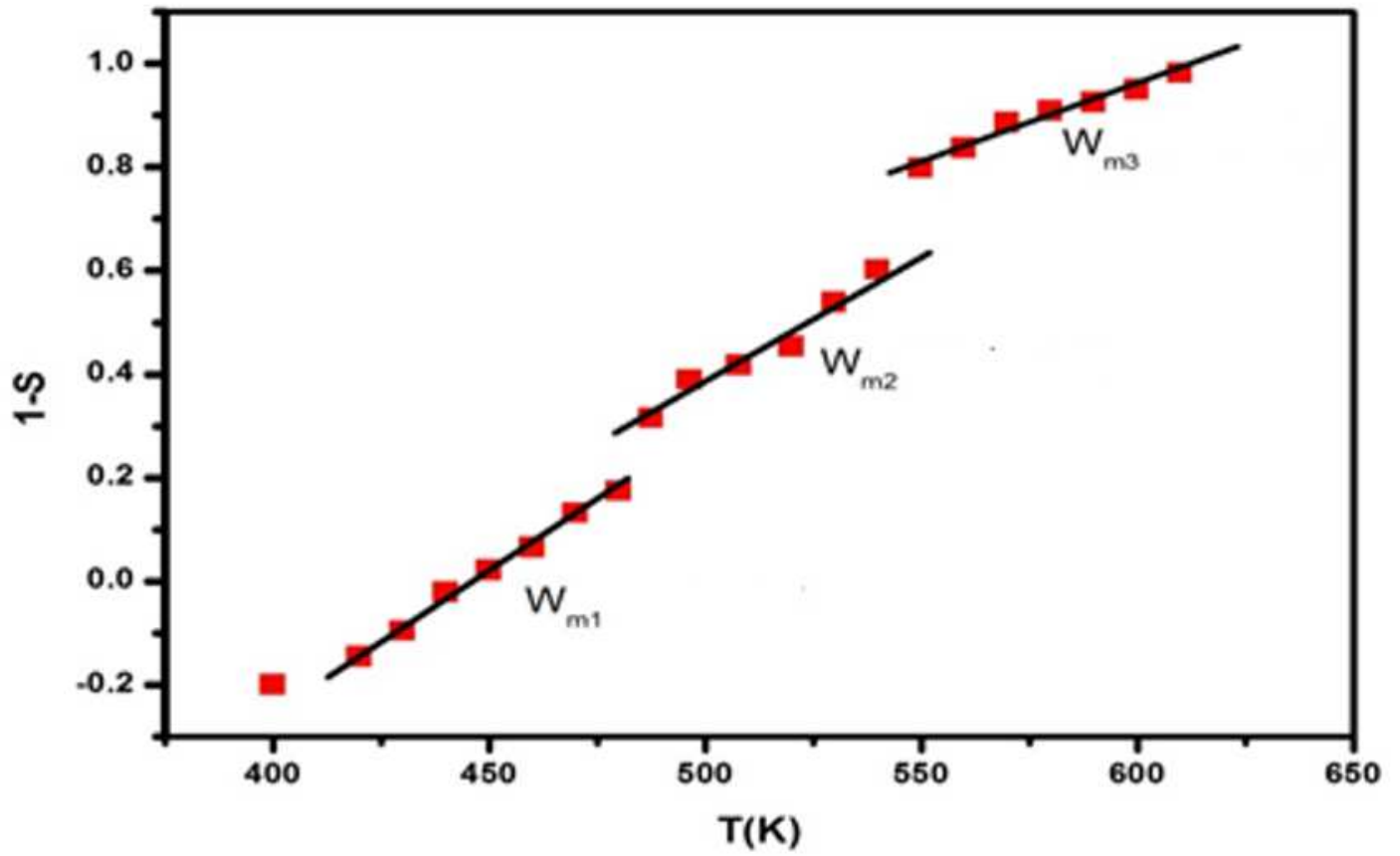


Figure 8

Variation of $(1-s)$ with temperature of In_2S_3 film deposited on ITO substrate.

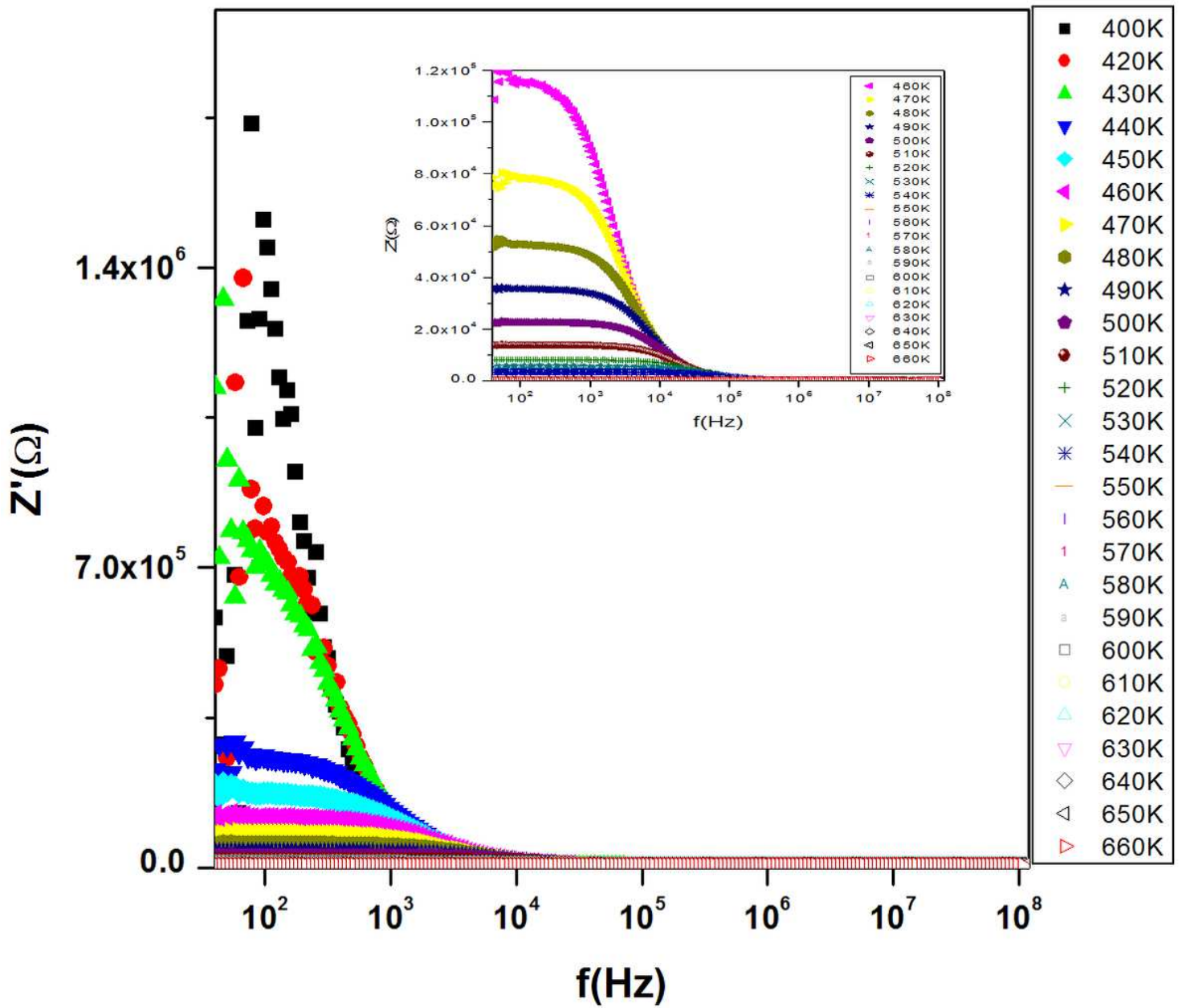


Figure 9

Variation of the real part Z' of impedance as a function of frequency at different temperatures for In_2S_3 film deposited on ITO substrate.

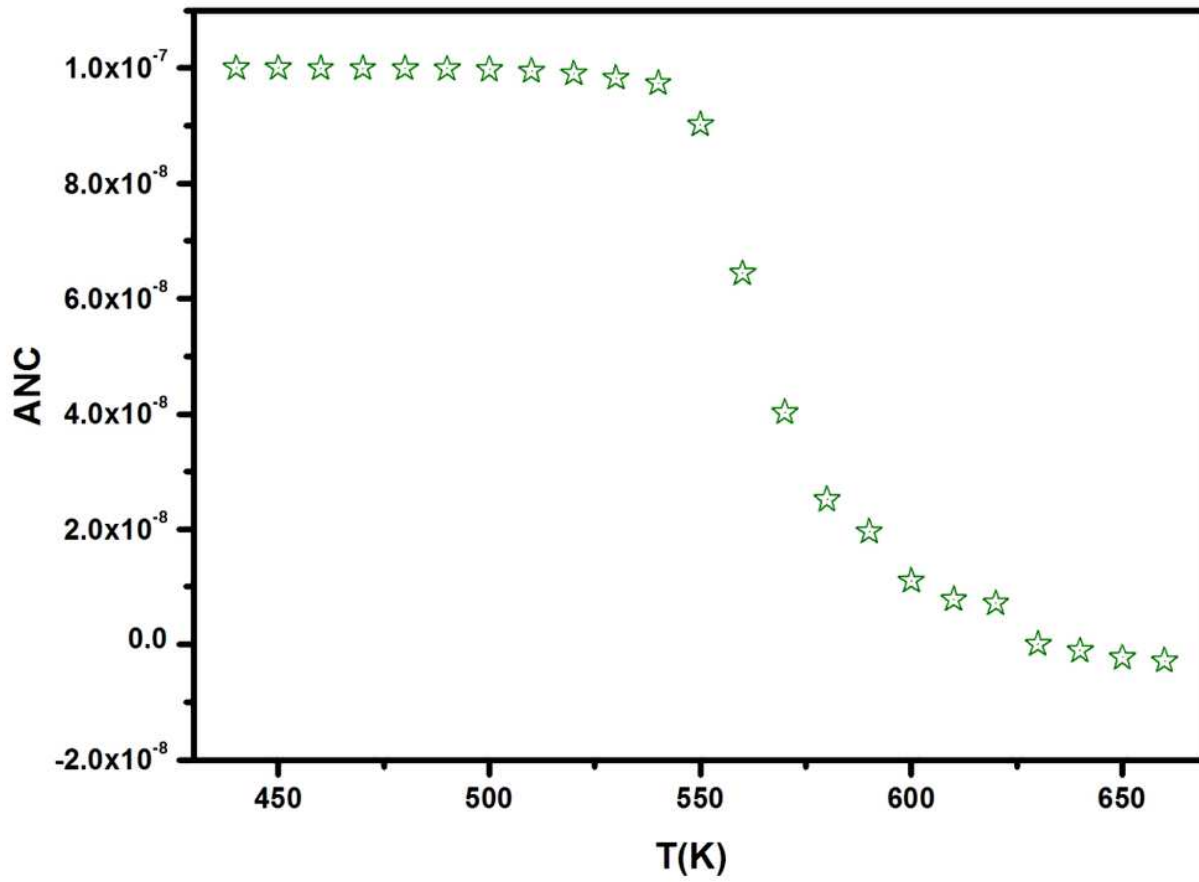


Figure 10

Average normalized change ANC with temperature for In₂S₃ film deposited on ITO substrate.

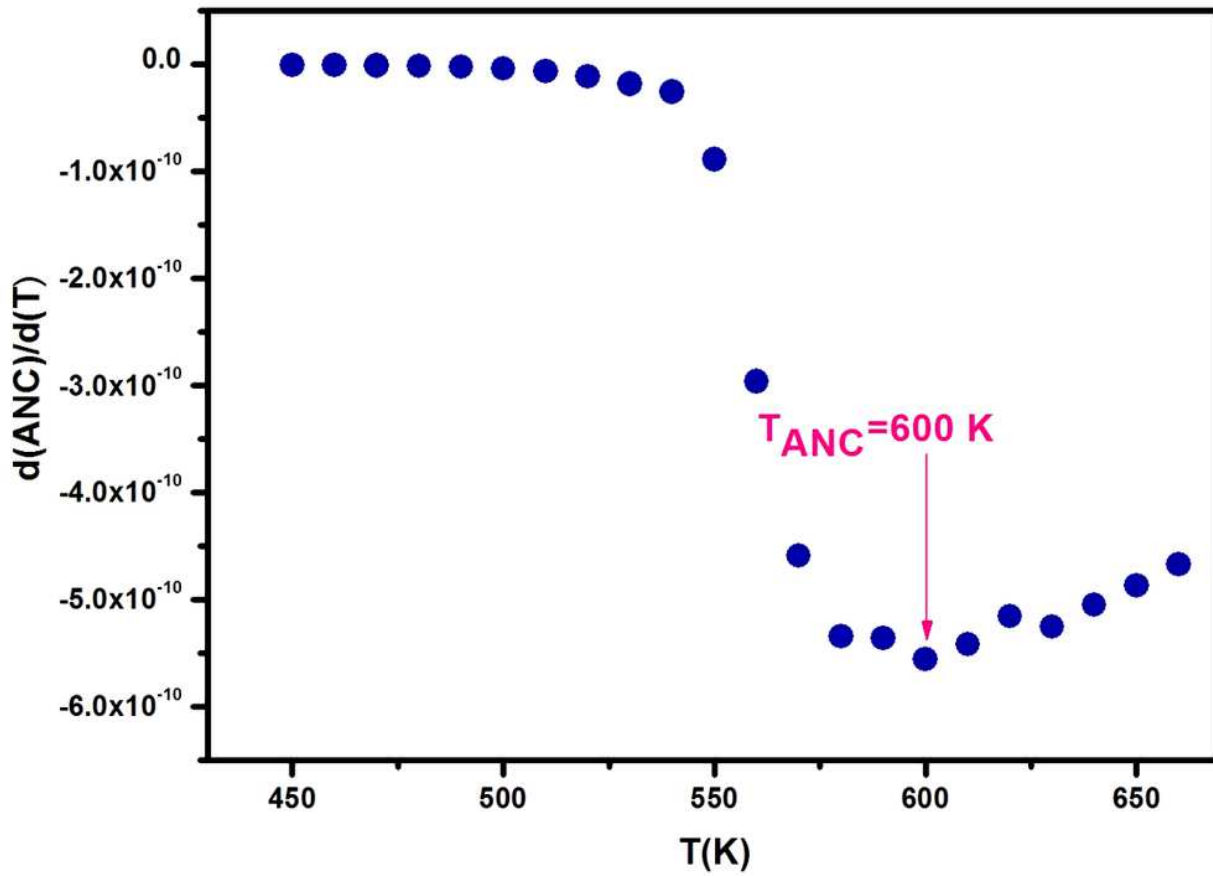


Figure 11

Variation of $d(\text{ANC})/d(T)$ with temperature for In_2S_3 film deposited on ITO substrate.

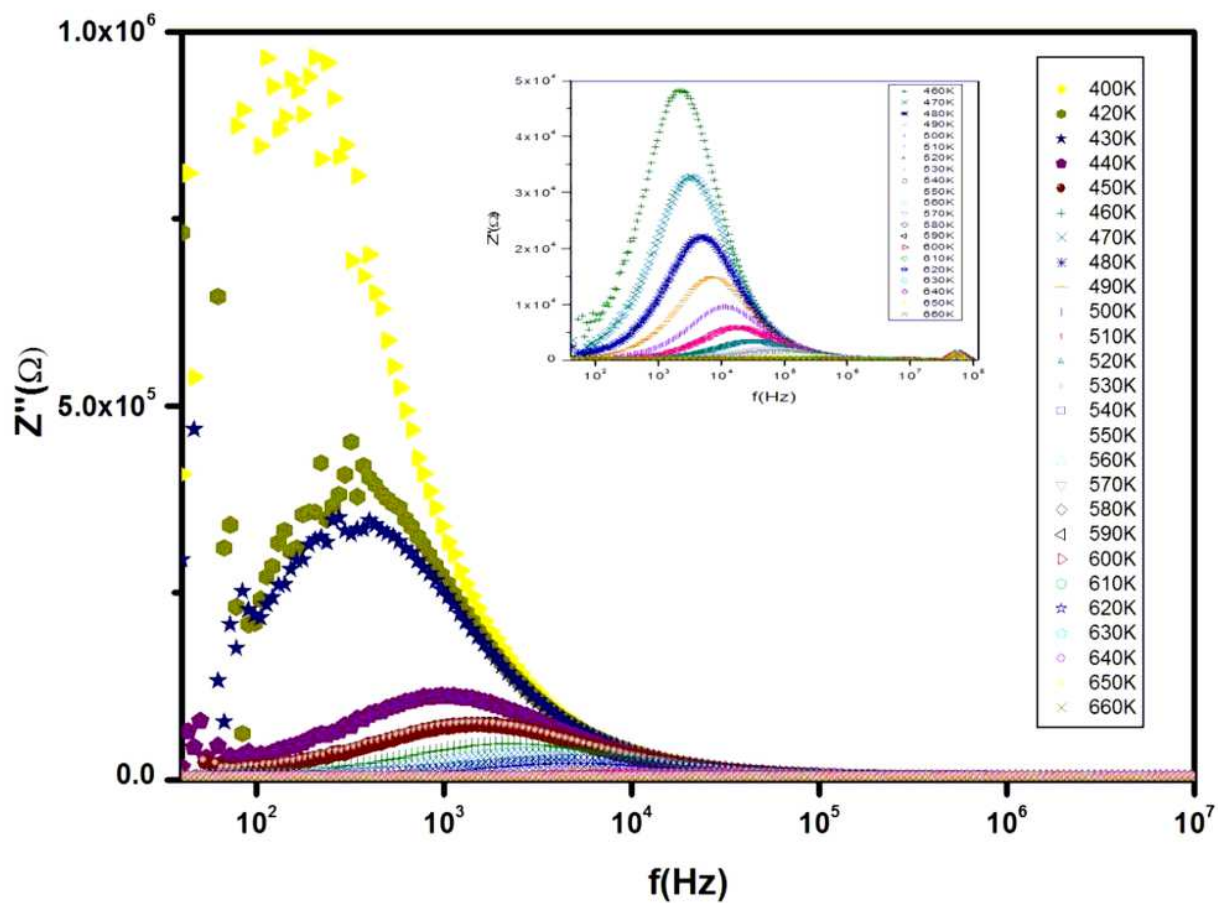


Figure 12

Variation of the imaginary part Z'' of impedance as a function of frequency at different temperatures for In_2S_3 film deposited on ITO substrate.

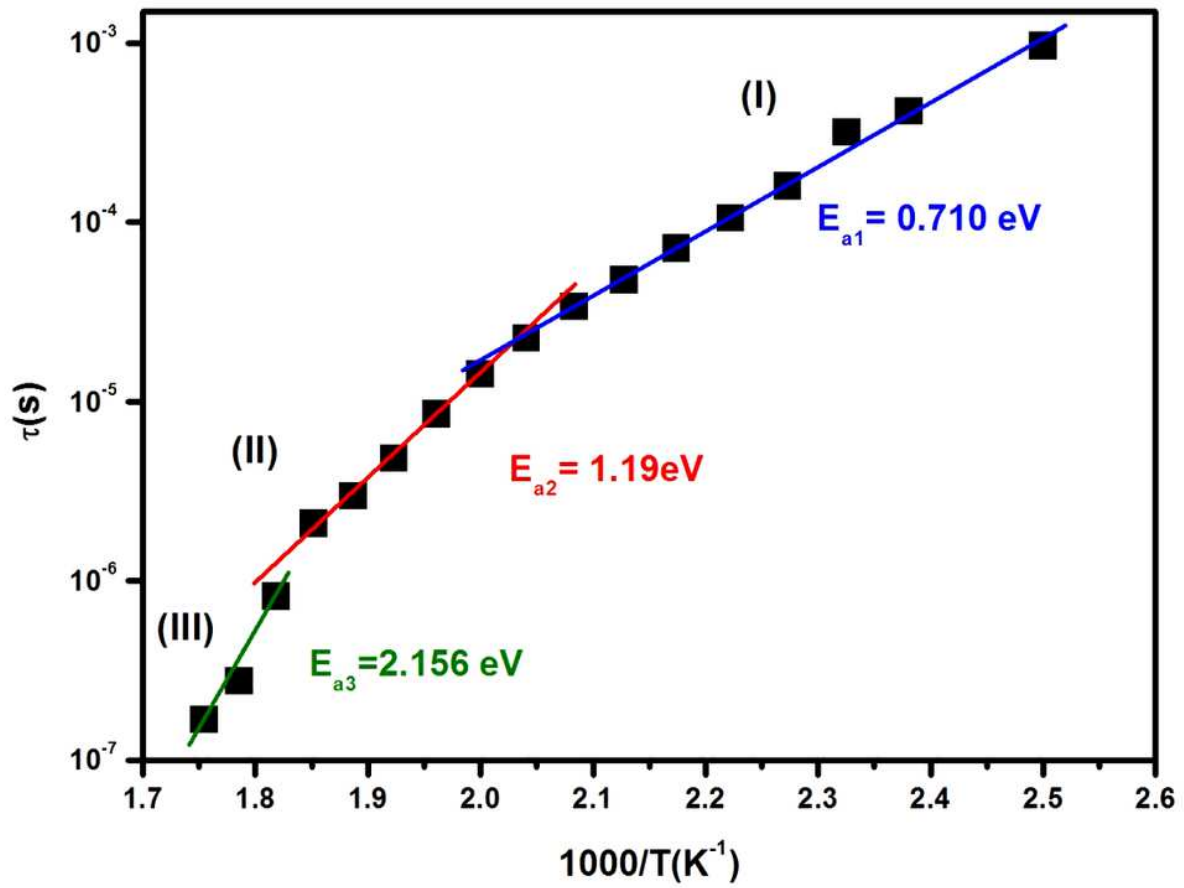


Figure 13

Arrhenius plot of time relaxation.

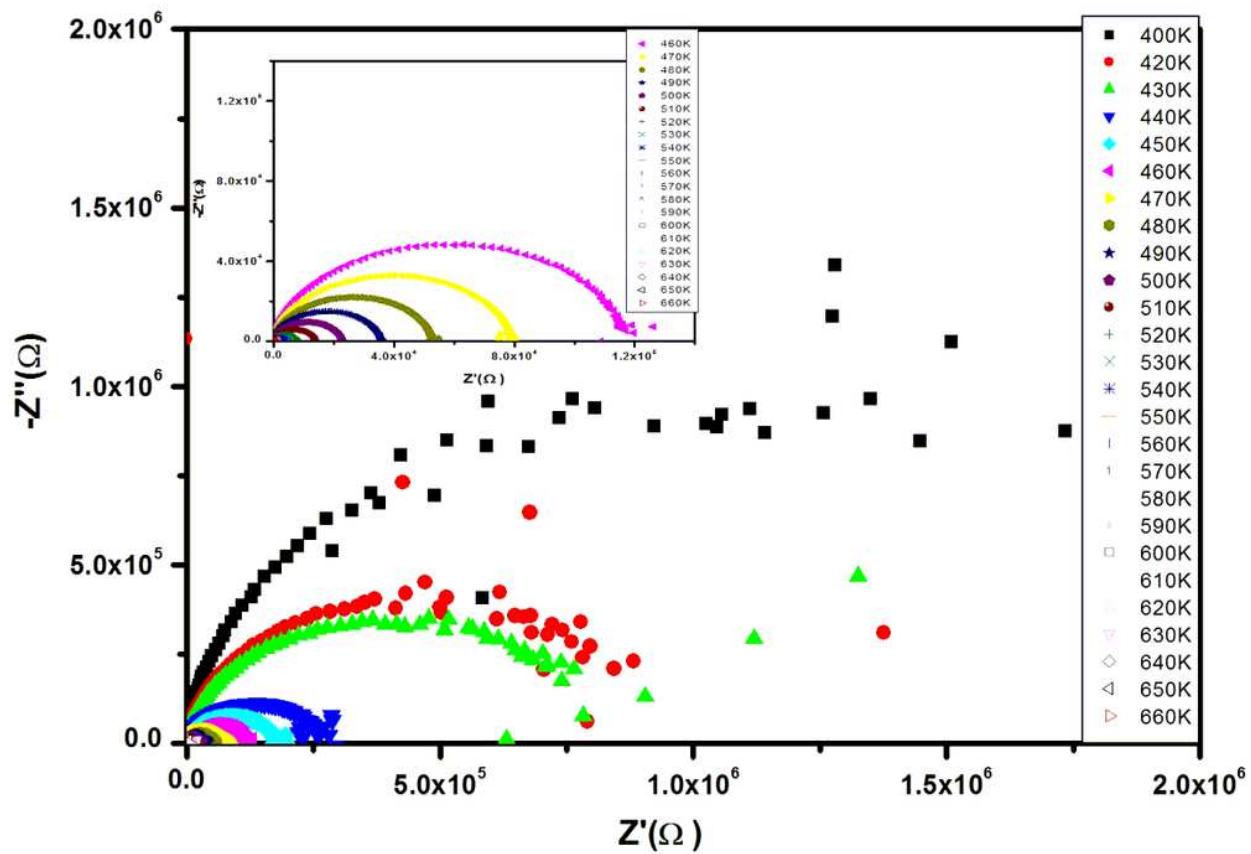


Figure 14

Complex impedance spectrum (-Z'' vs. Z') of In₂S₃ film deposited on ITO substrate.

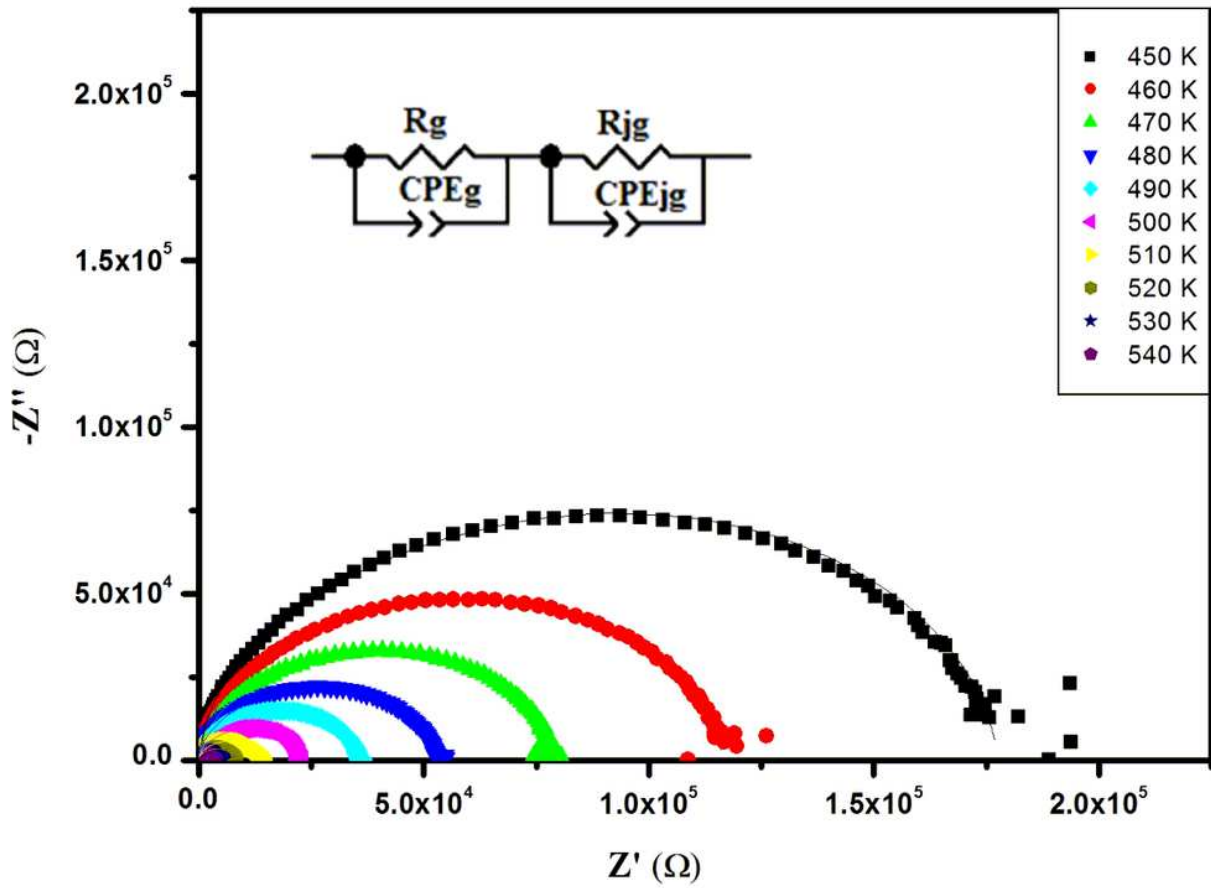


Figure 15

Results of fitting of the Nyquist diagram and equivalent circuit model for In_2S_3 film deposited on ITO substrate.